Chemosphere 242 (2020) 125259

Contents lists available at ScienceDirect

Chemosphere

journal homepage: www.elsevier.com/locate/chemosphere

Loofah-derived activated carbon supported on nickel foam (AC/Ni) electrodes for the electro-sorption of ammonium ion from aqueous solutions

Yu-Jen Shih [a], [**], Cheng-Di Dong [b], Yao-Hui Huang [c], C.P. Huang [d], [*]

[a] *Institute of Environmental Engineering, National Sun Yat-sen University, Kaohsiung, 804, Taiwan*
[b] *Department of Marine Environmental Engineering, National Kaohsiung University of Science and Technology, Kaohsiung, 811, Taiwan*
[c] *Department of Chemical Engineering, National Cheng-Kung University, Tainan, 701, Taiwan*
[d] *Department of Civil and Environmental Engineering, University of Delaware, Newark, DE, 19716, USA*

HIGHLIGHTS

- Dried loofah sponge was used to prepare activated carbon successfully.
- One step activation without pre-pyrolysis yielded activated carbon of high specific capacity.
- Activated carbon-nickel foam (OAC/Ni) electrode exhibited 80% charge efficiency.
- OAC/Ni electrodes yielded a maximum ammonium adsorption capacity of 6 mg-N g^{-1}.

GRAPHICAL ABSTRACT

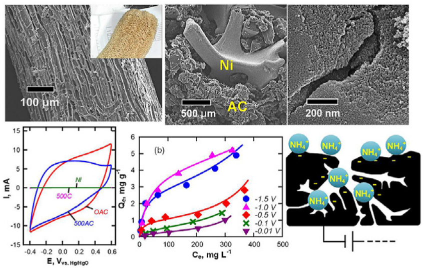

ARTICLE INFO

Article history:
Received 6 August 2019
Received in revised form
17 October 2019
Accepted 28 October 2019
Available online 31 October 2019

Handling Editor: E. Brillas

Keywords:
loofah sponge
Specific capacitance
Activated carbons
Electrosorption
Ammonium

ABSTRACT

Activated carbon (AC), prepared from dried loofah sponge, was supported on nickel foam to fabricate AC/Ni electrodes. The characteristics of ammonium electrosorption on AC/Ni electrodes was studied. Results showed that AC prepared in one-step activation (without pre-pyrolysis), i.e., OAC, had relatively low crystallinity, high mesoporosity, and high specific capacitance compared to those made in two-step carbonation followed by activation. Adsorption and desorption density of NH_4^+ were measured at constant potential of −1.0 V (vs. Hg/HgO) and +0.1 V (vs. Hg/HgO), respectively. Non-faradaic charging contributed to the electrochemical storage and adsorption of ammonium ions on the AC surface with a maximal charge efficiency of 80%, at an applied potential of −1.0 V (vs. Hg/HgO). Multiple-layer adsorption isotherm better described the electrosorption of ammonium ion on OAC/Ni electrodes yielding a maximum adsorption capacity of 6 mg-N g^{-1}, which was comparable with other similar systems. Overall, results clearly demonstrated the effect of synthesis strategy on the capacitive charging behaviors of AC/Ni electrodes and its relationship to NH_4^+ electrosorption.

1. Introduction

Excessive ammonium/ammonia (NH_4^+/NH_3) nitrogen in natural waters is a growing concern due to its detrimental impact on aquatic ecosystems. The presence of nutrients, such as ammonium,

---

[*] Corresponding author.
[**] Corresponding author.
E-mail addresses: yjshih@mail.nsysu.edu.tw (Y.-J. Shih), huang@udel.edu (C.P. Huang).

https://doi.org/10.1016/j.chemosphere.2019.125259
0045-6535/

nitrate, and phosphate, in natural waters causes algal blooms, a process known as eutrophication, can deplete dissolved oxygen, and release toxins to the surrounding water environment. Generally detergents, fertilizers, and municipal sewage effluents are major sources of nitrogenous compounds. Ammonia-nitrogen ($NH_4^+/NH_3{-}N$) is the main degradation byproduct of nitrogenous organics, such as azo dyes, organic solvents, and pharmaceuticals, during wastewater treatment. The Urban Waste Water Directive (92/271/EEC) of the European Water Framework Directive (2000/60/EC) has recommended a discharge limit of 10 mg-N-L^{-1} in ecologically sensitive areas (Hauck et al., 2016).

Several methodologies could practically reduce the NH_4^+/NH_3 level in aqueous solution, including struvite precipitation, air striping, microbial oxidation, electrochemical oxidation, breakpoint chlorination, and adsorption or ion exchange, depending on the total ammonium concentration among other parameters such as pH (Sarvajith et al., 2018; Ye et al., 2018; Song et al., 2019). NH_4^+ can be converted to non-toxic N_2 by either direct oxidation over specific electrodes or chlorine indirectly yielded from the electrolysis of chloride ions. We have demonstrated recently that nickel oxide and lead dioxide anodes can efficiently mediate the electron transfer of ammonium in dilute concentrations (<20 mg-N L^{-1}) (Shih et al., 2017, Shih et al., 2018[1], Shih et al., 2018). However, the selectivity of NH_4^+ conversion to N_2, NO_2^- or NO_3^- is pH- and potential-dependent. Breakpoint chlorination by anodic oxidation of Cl^- aids nitrogen selectivity. But there are needs for electrodes of high reactivity and corrosion resistance. Additionally, the generation of secondary chlorinated pollutants is a technical challenge for the water quality management program, especially when excessive chlorine is produced (Garcia-Segura et al., 2018). Since under ambient conditions, ammonium is the dominant inorganic nitrogen species ($pK_a = 9.25$), therefore, electrostatic attraction can be effective for ammonium removal from waters (Zhang et al., 2011). Consequently, capacitive deionization (CDI) has emerged as a robust, energy- and cost-effective method for the desalination of seawater and brackish water (Porada et al., 2013; Kumar et al., 2016). Electrical double layer (EDL) formation over the porous surface of carbon materials in the presence of an electrical field is the major mechanism of ions storage, and thus removal, in CDI process (Laxman et al., 2014). Contrast to conventional ion adsorption, CDI, electrodes can be readily regenerated and the adsorbed ions are instantaneously released to the bulk solution by reversing the polarity of the applied voltage (Kim et al., 2015). In the absence of chemical reactions, specifically at low overpotential when electron transfer between the electrode and electrolytes is slow (Avraham et al., 2010), electrosorption becomes a purely physical process that enables long service life and low maintenance of CDI devices. Moreover, in contrast to anodic oxidation that completely converts NH_4^+ to N_2, CDI produces concentrated ammonium solution during the regeneration stage, which enables NH_4^+ recycle Ammonia solution at high concentration is idea electrolytes for fuel cells applications as it is carbon-free, easy to store and transport, less flammable than hydrogen fuels and relatively safe (Afif et al., 2016).

There have been extensive research activities, since the 1990s, on developing effective carbon materials of high specific surface area for deionization. Among an extensive array of materials covering activated carbons, tunable carbide-derived carbons, nanotubes, and graphene (Wimalasiri et al., 2015; Lee et al., 2018), porous carbons, e.g., activated carbon (AC) are by far the most commonly used because of cost effectiveness for capacitive deionization (CDI) applications. AC can be made from a long list of naturally occurring and synthetic carbonaceous precursors, including low-grade carbon minerals (bituminous coal, anthracite) (Teng and Yeh, 1998; Lozano-Castello et al., 2001) and plants (corn cob, wood, coconut shell) (Thakur et al., 2017; Danish and Ahmad, 2018). It is known that the type of raw materials can influence the quality, characteristics, and properties of the AC toward ion adsorption. Agricultural byproducts or waste residues are ideal AC precursors (Suhas et al., 2016), renewable and economic lignocelluloses materials, have received the most attention for AC preparation. For example, dried Loofah, a typical agricultural waste product, can be ideal raw material for the synthesis of biochar and activated carbon. The ash content of dried loofah was less than 1 wt %, lower than most known agriculture waste residues, which implies that this raw material has higher carbon purity, making it an ideal candidate for AC preparation (Shih et al., 2019). CDI process has been studied extensively for the electrosorption of simple salts such as NaCl (Li et al., 2018), other inorganic salts such as transition metal ions, oxyanions, and organic acids using activated carbon as electrode materials (Tang et al., 2015; Huang et al., 2016; Dai et al., 2018; Park et al., 2018), but limited information is available on the preparation of carbon-based electrodes using agricultural residues and application of such electrodes for the electro-adsorption of weak Brønsted acid, such as NH_4^+.

It is hypothesized that the preparation procedure of AC, specifically, temperature and the mode of activation play a role on controlling the surface properties of biochar/activated carbon, thereby affecting the electrosorption of ions. In the present research, Ni foam-based activated carbon (AC/Ni) electrodes were prepared from a vegetable sponge (dried loofah) and the adsorption characteristics of ammonium ions (NH_4^+) from dilute aqueous solutions was studied. The AC adsorbents were characterized by X-ray diffractometer (XRD), scanning electron microscope (SEM), and BET specific surface area measurements. The performance of the AC/Ni electrodes was first determined in terms of electrical capacitance using a potentiostat. The adsorption isotherm of ammonium ion on AC/Ni electrodes was obtained under constant potential mode and the maximum ammonia adsorption capacity was determined. The effect of ionic strength on ammonium electrosorption was studied by applying the Stern-Gouy-Chapmann version of electrical double layer theory.

2. Materials and methods

2.1. Chemicals

An agricultural residue, dried ripened fruit of *Luffa cylindrica*, i.e., loofah sponge, was used as the raw material to synthesize activated carbon. Loofah is the fruit of *Luffa aegyptiaca,* a sponge gourd. It is an annual vine, native to South and Southeast Asia. Commonly, waste loofah, after being dried to form fibrous network, is used as bath or kitchen sponge. The nickel foam (sheet thickness = 2 mm, area density ~ 250 g m^{-2}, 94 ± 10 mesh), a porous substrate for immobilizing the AC sample, was purchased from Innovation Materials Co., Ltd., Taiwan. Deionized water further purified with a laboratory-grade RO-ultrapure water system (resistivity >18.18 MΩ cm), was used for the preparation of all solutions. Zinc chloride ($ZnCl_2$, from Sigma-Aldrich Co., USA) was the activating agent for AC preparation. The stock ammonium solution was prepared with ammonium sulfate, $(NH_4)_2SO_4$, (J.T. Baker, USA). Sodium sulfate (Na_2SO_4, Sigma-Aldrich Co., USA) was used as the supporting electrolyte. The solution pH was adjusted to a specific value with sodium hydroxide (NaOH, Merck KGaA, Germany) and sulfuric acid (H_2SO_4, 95%, Sigma-Aldrich Co., USA). Chemicals for the analysis of ammonia-nitrogen included sodium hypochlorite (NaClO), sulfanilamide ($H_2NC_6H_4SO_2NH_2$), sodium phenoxide

---

[1] (Shih et al., 2017, Shih et al., 2018a, Shih et al., 2018b)

($NaOC_6H_5 \cdot 3H_2O$) (Sigma-Aldrich Co., USA), and sodium nitroprusside ($Na_2[Fe(CN)_5NO]$) (Riedel-deHaën AG, Germany). All reagents were of analytical grade and used without purification.

2.2. Experimental procedure

The fibrous cushion of loofah sponge, cut into pieces of 2 cm × 2 cm in size, was first washed with acetone and deionized water (Fig. S1a) and then dried at 105 °C overnight. Biochar was prepared by pyrolysis, under nitrogen, of dried raw loofah at 300, 400, and 500 °C, and designated as 300C, 400C and 500C, respectively. To prepare activated carbon, raw loofah and biochar 300C, 400C and 500C were thoroughly mixed with $ZnCl_2$ at a mass ratio of 4:1 ($ZnCl_2$ to C). Table 1 shows that increasing the pyrolysis temperature increased the fixed carbon content due to loss of volatile matters (weight loss increases as temperature increases). The mixture was preheated at 110 °C to remove water solvent and then added the activation agent, i.e., $ZnCl_2$. The black char became eventually sticky and was then transferred to a tubular furnace to start the pyrolysis process under N_2 atmosphere by heating to 800 °C at a heating rate of 5 °C-min^{-1} for 2 h (Hameed et al., 2007). The AC products were denoted as OAC, 300AC, 400AC, and 500AC, respectively. (Note that OAC was prepared directly from dried raw loofah without pre-pyrolysis.) To remove the unreacted chemical reagents, all AC samples were washed with 0.5 M of HCl and deionized water for several times until the pH of the rinse reached around 7.

The AC slurry, prepared by mixing AC (3 g) with poly(vinylidene fluoride) (PVDF) as binder (~5 wt%) and *n*-Methyl-2-pyrrolidone (NMP) as solvent (Sigma-Aldrich Co., USA), was then uniformly applied on the nickel foam (Fig. S1b). NMP was vaporized at 105 °C in a vacuum oven as to obtain the AC/Ni electrode. Then AC/Ni was rolled into a cylinder, 7.5 cm in length and 3.5 cm in diameter (geometric area ~80 cm^2), and used as a working electrode. The counter electrode, a Ti/IrO_2 cylinder 5 cm in diameter, was placed around the working electrode at the concentric location; the average electrode-to-electrode distance was 0.5 cm. Note that Ti/IrO_2 has been used as anode or cathode for the treatment of a variety of pollutants with excellent stability (Shih et al., 2014, Shih et al., 2018, Shih et al., 2018; Cheng et al., 2017).) Electrochemical experiments were carried out with a potentostat (CHI611C, CH Instruments, Inc., USA) and a reference electrode, Hg/HgO/1 M NaOH ($E^0 = 0.14$ V vs. NHE) (RE-61AP, ALS Co. Ltd., JAPAN). Prior to experiments, the AC/Ni electrode was soaked in 0.5 M NaOH overnight to increase the hydrophilicity of the surface. Note that the hydrophobicity of carbon/PVDF composite was moderately reduced after alkaline treatment due to the formation of hydroxyl groups (Boo et al., 2016). Fig. S1c shows the configuration of the electrochemical cell. The ammonium adsorption isotherm was obtained in batch mode at initial ammonium concentrations of 20–500 mg-N L^{-1} and constant potential of −1.0 V (vs. Hg/HgO) for 80 min during electrosorption and then at +0.1 V (vs. Hg/HgO) for 40 min during desorption.

Table 1
Properties of dried loofah and weight loss of pyrolyzed carbons, and the corresponding BET results in comparison with those of activated carbons.

	Ash content, %	Moisture, %	Weight loss, %
Original loofah	0.64%	9.7%	
300C			44.2 ± 7.6
400C			71.2 ± 0.38
500C			76.8 ± 0.51
	S_{BET}, m^2 g^{-1}	Pore volume, m^3 g^{-1}	Pore size, nm
Original loofah	0.85	0.001	6.84
300C	2.41	0.004	5.56
400C	3.23	0.003	3.61
500C	7.61	0.006	3.45
OAC	1606	1.04	2.58
300AC	1600	1.19	2.99
400AC	1594	0.84	2.11
500AC	978	0.41	1.66

2.3. Analyses

A flow injection analyzer (FIA, Lachat's Quik Chem 8500 Series 2, USA) based on the Berthelot reaction was used to analyze the concentration of aqueous NH_4^+. The indophenol method (at 630 nm) was a catalytic reaction involving phenolate, hypochlorite, and ammonia, with nitroprusside as the catalyst (Stewart, 1985); the detection limit was 0.2 μg L^{-1} for NH_4^+-N.

The surface morphology of AC/Ni electrodes was characterized by scanning electron microscopy (SEM, JSM-6700F, JEOL Ltd., Japan). The crystallographic structure was detected by X-ray diffraction (XRD, DX III, Rigaku Co., Japan) operated with Cu Kα source ($\lambda = 1.5406$ Å) at a scan rate of 0.06° s^{-1} at an incidence angle range of 20–85° (2θ). Raman spectra were obtained using a DXR™ microscope (Thermo Fisher Scientific Inc., USA). The Brunauere Emmette Teller (BET) surface area, total pore volume, and mean pore diameter were measured using a surface area/porosity analyzer (Micromeritics ASAP).

3. Results and discussion

3.1. Properties of AC derived from dry loofah sponge

Table 1 summarizes the porosity characteristics in terms of surface area, pore volume, and pore size distribution of raw loofah, biochar (300C, 400C, and 500C), and activated carbon (OAC, 300AC, 400AC, and 500AC), individually. The dried loofah and carbonized char were typically non-porous materials (BET specific surface areas < 10 m^2-g^{-1}). After activation, the specific surface area reached 1600 m^2-g^{-1} by either one-step (OAC) or two-step (300AC) activation at low pre-pyrolysis temperature. However, the specific surface area was apparently reduced to <1000 m^2-g^{-1} when the pyrolysis temperature was increased to 500 °C. Fig. 1a shows the BET adsorption isotherm of the carbonized (500C) and activated samples (AC). According to IUPAC classification, N_2 adsorption on OAC and 300AC belonged to the IV-type adsorption isotherm; whereas increasing the carbonization temperature, N_2 adsorption on 400AC and 500AC was a mixture of type I and II isotherms (Alothman, 2012; Yuan et al., 2018). The result demonstrated that pre-pyrolysis might modify the shape and pore size distribution. The 400AC and 500AC samples were highly microporous materials, which external surface was reduced at elevated temperature. Moreover, the marked hysteresis loop of N_2 desorption on OAC and 300AC clearly indicated the presence of mesopores (Hu et al., 2001). It is noted that although only a small amount of PVDF, ca. ~5%, was used as binder, potential pores blockage might occur to some extent (Lacey et al., 2014). The BET area of AC on the Ni foam could not be measured accurately, however.

b presents the Raman spectra of the AC samples. Two main broad peaks of G band at 1576.1 cm^{-1} and D band at 1250–1450 cm^{-1} appeared on the carbon surface. G and D band indicated the presence of graphitic crystalline structure from the stretching vibration of the sp^3/sp^2 orbitals of carbon atom on the aromatic hexagonal sheet and disordered lattice with vacancies in aromatic ring lamellae, respectively (Diehl et al., 2013). The intensity ratio of (I_D/I_G) is a measurement of zone edges of clusters; decrease in I_D/I_G ratio improves the ordered regions of the graphitic cluster sizes in a complete sp^2 network and *vice versa*. The ratio of

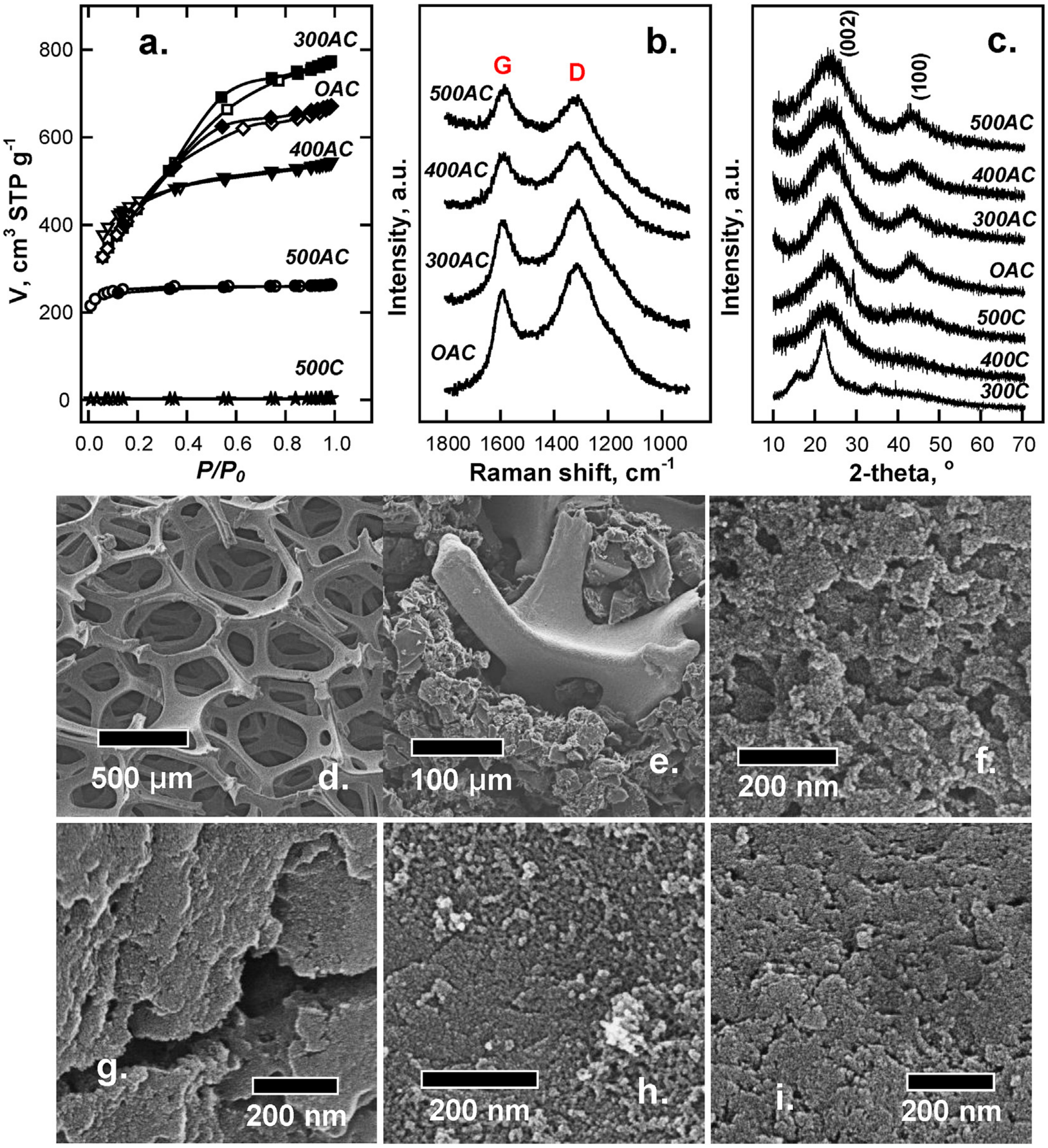

Fig. 1. (a) N_2 adsorption-desorption isotherms, (b) Raman spectra, and (c) XRD patterns of pre-pyrolyzed carbon and activated carbons. SEM micromorphology of (d) nickel foam, (e) AC/Ni, and activated carbons of (f) OAC, (g) 300AC, (h) 400AC and (i) 500AC.

I_D/I_G followed the order: OAC (1.19) > 300AC (1.11) > 400AC (1.05) > 500AC (0.96), which suggested an increase in the crystallinity of carbon with increase in temperature. Without activation, the XRD pattern of the carbonized sponges displayed a diffraction peak of (002) plane at 26° (Fig. 1c), predominantly ascribed to the formation of graphitic sheet (Ariharan et al., 2016). The broad peak at around 44° 2θ appeared on 300AC-500AC samples was due to the overlapping of (100) and (101) planes created by sp^2 hybridized carbons, called turbostratic structure. In other words, structures of all activated carbon materials were intermediates between graphite and carbon with a random layer lattice (Simaioforidou et al., 2017). Pre-pyrolysis of loofah at high temperature (300–500 °C) may lead to partial sintering and structural relaxation and result in an increase in carbon crystallinity with reduced surface area (Zhou et al., 2015). Further, the surface area of unstructured char that underwent an activation process at 800 °C was improved through the exposure of new micropores. Accordingly, AC as a capacitive material will acquire simultaneously proper crystallinity, which enhances the electrode conductivity and high specific surface area necessary for the accommodation of more ions in question. Both XRD and Raman results confirmed improvement in long-range ordering of graphene sheets with the extent of volatile matter burn-off. Nevertheless, carbonization during pre-pyrolysis may adversely influence the creation of mesoporosity. From the SEM micro-texture of ACs/Ni as shown in Fig. 1d–i, Ni foam was selected as electrode support mainly because of its unique pentagonal framework in the size of 50–250 µm. It is known that 3-D porous metallic electrodes outperform 2D plates and sheets due to superior surface area, which enhances mass transfer efficiency (Tan et al., 2018; Arenas et al., 2019). In this work, AC particles were intercalated into the vivid open pores of Ni foam with a small amount of PDVF binder, which further improved the contact between the electrode and electrolytes. In particular, OAC and 300AC samples had a large number of macro-size cavities. Increasing the carbonization temperature (e.g., 400 and 500 °C) decreased the size of micropores. Obviously, the intercross-pores contracted at high temperature and hence reduced porosity (Allwar et al., 2008; Wrobel-Iwaniec et al., 2015).

3.2. Electrochemical characteristics

Cyclic voltammetry (CV) was used to assess the electrochemical characteristics of Ni foam-based carbon electrodes in the potential window of -0.4 to $+0.6$ V (vs Ag/AgCl) as shown in Fig. 2a–d. Fig. 2e gives the specific capacitance in Na_2SO_4 electrolyte (at pH ~ 7). Carbonized char of loofah (500C/Ni) was not a good capacitor due to low current response (Fig. 2a). Generally, the current profile, with the scan voltage in the anodic and cathodic direction also symmetrical with respect to applied voltage, E, was due to the capacitive charging by sulfate and sodium ions, respectively (e.g. CV of OAC/Ni, Fig. 2b). However, as reflected by the triangular CV of 500AC/Ni (Fig. 2c), less ion charging occurred, suggesting reduction of oxygen groups (-C=O, -C-O) during negative potential scan. The redox transition of quinone and hydroquinone groups on the edge of graphene sheet was known to be responsible for pseudo-capacitive reaction of carbon (Golub et al., 1987; Avraham et al., 2010). In other words, pre-pyrolysis in the two-step activation method may create more oxygen-containing groups on AC surface. In the absence of strong reducing agent such as hydrogen, oxygen-containing groups, specifically, carboxyl, carbonyl, phenols, and lactone, originated from the carbon precursor during activation, were derived (Yahya et al., 2015). The influence of the solution composition and concentration on charging capacity was assessed further by comparing the CV profile of Ni, 500C, OAC, and 500AC in different electrolytes (Fig. 2d). The metallic Ni subtract exhibited no capacitive current in the selected potential window, which was evidence of current magnification by charging of the incorporated AC. In addition, based on the similarity in current profile between KCl and Na_2SO_4 electrolytes, the ions, namely, K^+, Na^+, Cl^- and SO_4^{2-}, were not specifically adsorbed on AC.

At a given potential scanning rate, ($v = dE/dt$, $E = E_i \pm vt$), the differential capacitance of the electrode, C, can be expressed by:

$$C \equiv \frac{d\sigma}{dE} = \frac{Idt}{dE} = \frac{I}{v} \tag{1}$$

where the surface charge density (σ, C-m^{-2}) is dependent on the surface potential (E) according to the principle of diffuse electrical double layer. Considering the Stern's modification for Gouy-Chapman model of electrical double layer (EDL), the total capacitance, C_T (F-m^{-2}), during ion charging, may be resolved in two components in-series, i.e., the capacitance at the outer Helmholtz plane (OHP), C_H, and the capacitance of the diffuse EDL, C_D, (Oren et al., 1984):

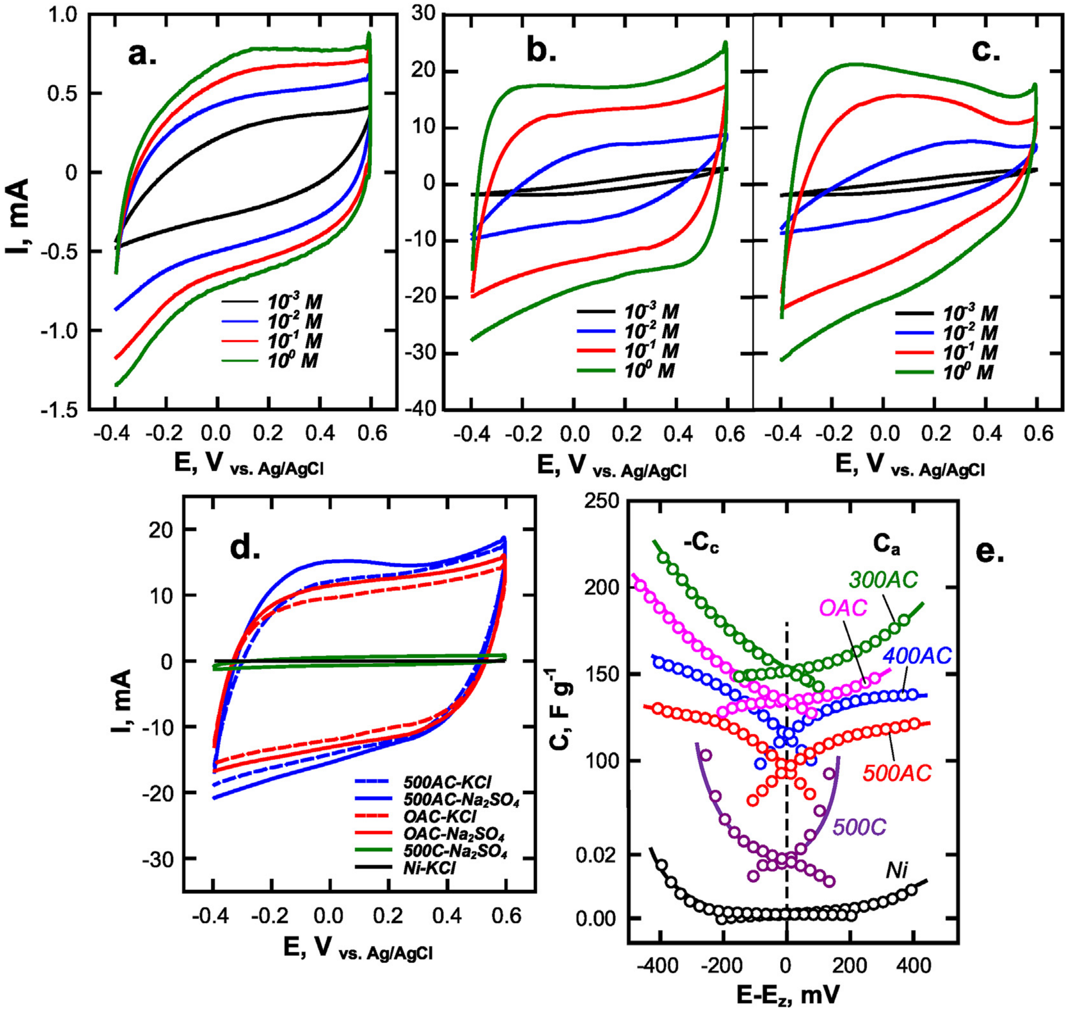

Fig. 2. CVs of (a) 500C/Ni (carbonized sponge), (b) OAC/Ni and (c) 500AC/Ni (activated carbon) in different electrolyte concentration (Na_2SO_4). (d) CVs and (e) differential capacitances in different types of inert electrolyte (concentration = 1 M, sweep rate = 2 mV s^{-1}, effective mass = 0.073 g for 300AC, 400AC and 500AC, and 0.067 g for 500C and OAC).

$$\frac{1}{C_T} = \frac{1}{C_H} + \frac{1}{C_D} \tag{2}$$

where

$$C_H = \frac{\varepsilon\varepsilon_0}{x_2} \tag{2a}$$

and

$$C_D = \sqrt{\frac{2\varepsilon\varepsilon_0 z^2 n^0 e^2}{k_B T}}\ \cosh\left(\frac{ze\varphi_2}{k_B T}\right) \tag{2b}$$

By substituting Eq. (2a) and Eq. (2b) into Eq. (2), one has:

$$\frac{1}{C_T} = \frac{x_2}{\varepsilon\varepsilon_0} + \frac{1}{\sqrt{2\varepsilon\varepsilon_0 z^2 e^2 n^0 / k_B T}\ \cosh\left(ze\varphi_2 / 2k_B T\right)} \tag{3}$$

where, φ_2 is the potential at plane x_2 of OHP, n_0 is the number concentration of electrolyte (cm^{-3}), and ε_0 and ε are vacuum permeability (8.854×10^{-12} $F\text{-}m^{-1}$) and relative permittivity of water medium (80 at 20 °C), respectively. C_H is constant and dominant at large electrolyte concentration and polarization; whereas, C_D varies, in V-shape, as a function of the potential. The differential capacitance can be obtained by separately plotting the anodic (I_a) and cathodic (I_c) current components against voltage sweeping rate, v, at different potential (the current was extracted from Fig. 2d). Since the capacitance obtained from anodic and cathodic sweeps were virtually symmetrical, the cathodic C_c was equal to but opposite in sign to the anodic C_a at potential of point of zero charge (E_{pzc}), that is, $C_a{}^\circ = {}^\circ d\cdot_+/dE = -d\cdot_-/dE = \text{-}C_c$ at $E = E_z$ (Omosebi et al., 2014; Shih et al., 2015). The differential capacitance approaches its minimum, i.e., C_{pzc}, at $E - E_z = 0$. The Ni foam and the 500C-electrode had a C_{pzc} value of 1.0 and 17.0 mF g^{-1}, respectively; whereas activation treatment substantially increased the C_{pzc} to 137, 150, 114 and 94 F g^{-1} for OAC, 300AC, 400AC and 500C, respectively, in 1 M Na_2SO_4 at pH ~7 (Fig. 2e).

Fig. S2 shows the C_{pzc} value as a function of ionic strength, I. The plot of C_d vs. $\sqrt{I}$ was in agreement with the following equation (Supporting Materials)

$$C_T = \frac{2.28 z \varepsilon_w \sqrt{I}}{2.28 z \delta \sqrt{I} + \varepsilon_w} \tag{4}$$

Note that C_d reaches a horizontal asymptotic vale of $C_T = \frac{\varepsilon_w}{\delta}$. From Fig. S2, the thickness of the Stern layer, δ, was estimated to be approximately equal to the hydrated ammonium ion radius of ~0.4 nm at STP (Chang et al., 2013; Brown et al., 2016).

In a CV process, the current, from charging the double-layer structure of carbon surface, was obtained at specific potential sweep rate. The porous property of electrode in a CDI system facilitated ion diffusion that subsequently enhanced its electrosorption capacity over specific time interval (Ma et al., 2017; Zornitta and Ruotolo, 2018). Accordingly, 500AC exhibited relatively smaller pore size, smaller specific surface area, and higher crystallinity than all other AC samples that were made from original loofah or carbonized chars at lower pyrolysis temperature. The differential capacitance ($F\text{-}g^{-1}$) at E_{PZC} followed the order: OAC ~ 300AC > 400AC > 500AC > 500C (Note that Eq. (4) may not properly hold for Fig. S2 when converting the unit of capacitance from $F\text{-}m^{-2}$ to $F\text{-}g^{-1}$ using BET specific surface area, since the surface area cannot be totally accessible to ions during charging.). Carbonization treatment in two-step activation diminishes the capability of electrochemical ion adsorption.

3.3. Electrosorption of NH_4^+

The performance of ammonium ion electrosorption on the AC/Ni electrode was investigated to illustrate the effect of carbon activation. Fig. S3 compares the adsorption and desorption of NH_4^+ as a function of time over four AC/Ni electrodes, namely, OAC, 300AC, 400AC, and 500AC. Results showed that NH_4^+ concentration decreased continuously during charging at −1.0 V (vs. Hg/HgO) and approached steady state in 80 min. High percentage of NH_4^+ adsorbed on the AC/Ni electrode was released readily into the solution by reversing the potential to +0.1 V (vs. Hg/HgO). The extent of ion desorption reached >80% rapidly in 40 min. It is noted that during discharging, the NH_4^+ concentration remained relatively unchanged, suggesting the absence of NH_4^+ oxidation. The adsorption isotherm, i.e., equilibrium NH_4^+ adsorption capacity (mg-N g^{-1}) versus equilibrium bulk NH_4^+ concentration (mg-N L^{-1}), was obtained to assess the maximum adsorption capacity and adsorption energy of NH_4^+ on the AC/Ni electrodes.

Fig. 3 shows the effect of AC type and working potential on electrosorption of NH_4^+. Generally, the adsorption isotherms did not follow simple Langmuir type due to the heterogeneity of porous AC. The adsorption energy might be different on porous surface. In other words, NH_4^+ filled up the external surfaces and mesopores first, then penetrated deeper into the micropores at higher NH_4^+ concentrations. According to the concept of multilayer adsorption, the total surface coverage of adsorbate (θ) in subsequent layers is as the following (Wang et al., 2015):

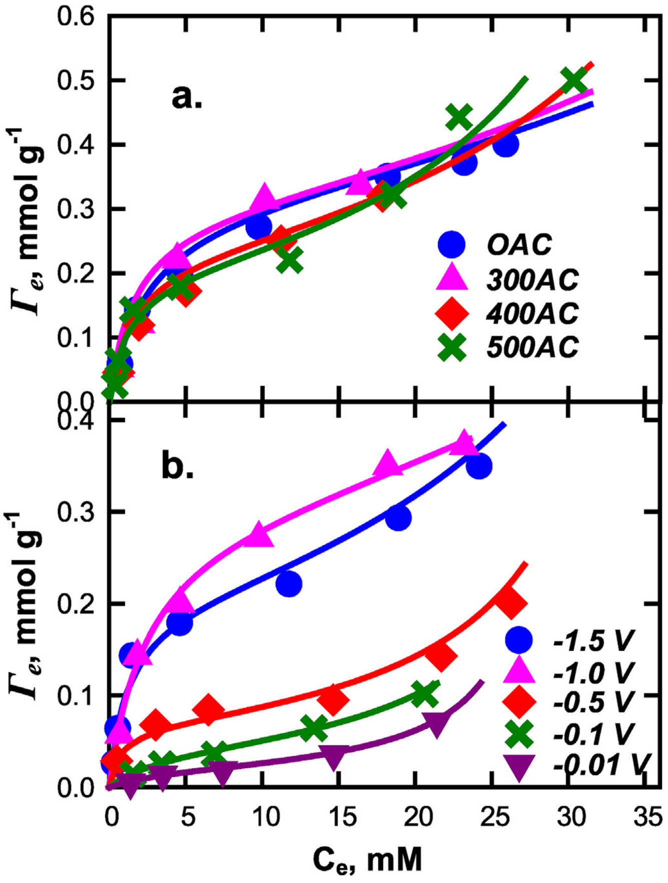

Fig. 3. Isotherms of ammonium adsorption using (a) different activated carbon electrodes at −1.0 V, and (b) different applied potential (vs. Hg/HgO) on OAC/Ni electrode (initial concentration = 20−500 mg-N L^{-1}; pH 7 (uncontrolled)).

$$\theta = \frac{K_1 C_e}{(1 - K_2 C_e)[1 + (K_1 - K_2) C_e]} \tag{5}$$

or

$$\Gamma_e = \frac{K_1 C_e \Gamma_1}{(1 - K_2 C_e)[1 + (K_1 - K_2) C_e]} \tag{5a}$$

where C_e = equilibrium NH_4^+-N concentration (mM), Γ_e = equilibrium NH_4^+ adsorption density (mmol g^{-1}), K_1 = equilibrium constant for the first layer adsorption (M^{-1}), K_2 = equilibrium constant for multilayer adsorption (M^{-1}), and Γ_1 = surface site density of monolayer coverage (mmol g^{-1}) for NH_4^+-N. Note that the first layer adsorption dominates if K_2 is relatively small compared to K_1, then Eq. (5a) can be simplified to the Langmuir equation, under which the capacity of the first-layer adsorption is close to the maximum monolayer adsorption capacity, Γ_m, according to the Langmuir adsorption isotherm.

Table 2 shows the parameter of electrosorption of NH_4^+ over AC/Ni. OAC/Ni exhibited the highest Γ_m of *ca.* 6 mg-N g^{-1} among all AC electrodes studied. Furthermore, increasing carbonization temperature decreased Γ_m and increased K_2. K_1 was one order of magnitude greater than K_2 and decreased slightly with increase in carbonization temperature. The change in equilibrium constant indicates variation in the Gibbs free energy of adsorption, i.e.:

$$\Delta G^0 = -RT \ln K \tag{6}$$

Table 2 shows the change of Gibbs free energy for the adsorption on the first layer and the second layer, respectively. Results showed that the free energy of adsorption was generally small, typical of electrostatic interaction. Note that low free energy of adsorption also favors desorption of adsorbed ammonium ion during discharging. It is interesting that the adsorption energy of the second layers was approximately one order of magnitude smaller than that of the first layer. In summary, pre-pyrolysis significantly affects the surface heterogeneity of the carbon. The evolved pores shrunk when most of volatile matters were removed during carbonization, when the activating agent was unable to fully swell the carbonaceous tissue during impregnation. The electrosorption isotherm further rationalized the microporous characteristics and relatively high crystallinity of the 500AC sample, when comparing with its mesoporous and more disordered OAC counterparts. Several parameters can affect ion selectivity (Helfferich, 1962). Kressman and Kitchner (1949) and Harned and Owen (1959) reported ion selectivity increase with increase in ionic radius, at least, among monovalent cations, e.g., $Li^+ < H^+ < Na^+$, $K^+ < Rb^+ < Cs^+$. The ionic radius of NH_4^+ is 175 pm which is larger than that of Cs^+ (167 pm). Accordingly, it is reasonable to suggest that NH_4^+ will have selectivity greater than that of Cs^+. In the absence of systematic comparison of ion selectivity of different ions, previously, the authors have studied NH_4^+ electro-sorption on AC/Ni electrode in the presence of different concentrations of supporting electrolyte, Na_2SO_4 and reported that competitive electro-sorption between NH_4^+ and Na^+ only became significant at Na_2SO_4 concentration of $>10^{-2}$ M (Shih et al., 2019).

Fig. 4a shows the current response at constant applied potential of −1.0 V (vs, Hg/HgO) (*i.e.* the amperometry) at different ammonium concentrations, $[NH_4^+] = 20–300$ mg-N L^{-1}. A high peak inrush current for OAC/Ni indicated higher capacitance, compared to the electrodes made by two-step activation. On the other hand, the working potential affected the equilibrium constant and adsorption capacity (Table 2). The Supporting Material (Fig. S4) gives the concentration profile of NH_4^+ as a function of adsorption time at different applying potentials (−0.01 to −1.5 V). The equilibrium NH_4^+-N concentration was used to plot the adsorption isotherm (Fig. 3b). Table 2 shows clearly that K_2 decreased and K_1 increased with increase in surface potential, which implied that the preference of NH_4^+ for the external surface was charged at higher applied potential.

Fig. 4b shows the temporary response of current as a function of time upon the application of charging and discharging voltage on the OAC electrode. Ammonium adsorption with charging time occurred when the electrode was negatively polarized at different cathodic potentials (from −0.01 to −1.5 V vs. Hg/HgO). The amount of ammonium adsorbed was readily desorbed from the OAC electrode during discharging by reversing the potential positively polarized (at +0.1 V vs. Hg/HgO). Different sign of current was created under corresponding charging/discharging run. One can obtain the total charge applied by integrating the current over time (in 1000s, Fig. 4b) to determine charge efficiency (η) (assuming purely non-faradaic current). Fig. 4c depicts the effect of potential on Γ_m, NH_4^+ removal (initial N = 50 mg-N L^{-1}), and charge efficiency (η), which was calculated according to Eq. (7):

$$\eta(\%) = \frac{z \times (X/M.w) \times F}{\int_0^t I dt} \times 100 \tag{7}$$

where z is the ion charge, X is the mass of nitrogen adsorbed (MW = 14), and F is the Faraday constant (96,485 C mol^{-1}). Γ_m was maximum at −1.0 V (~6 mg-N g^{-1}) when the adsorptive NH_4^+ removal and η were *ca.* 55% and 80%, respectively. A decline in bulk NH_4^+concentration, in terms of capacitive charging of ions, was definitely predominated by the electrical potential of the working electrode, while auxiliary reactions may be induced, which substantially impaired the current efficiency of non-faradaic charging. Carbon reduction ($C + H_2O + e^- = CH + OH^-$) and hydrogen gas

Table 2
Parameters of NH_4^+ adsorption isotherm on AC/Ni electrodes at different working potentials.

Samples[a]	K_1, M^{-1}	ΔG_1, kcal-mol^{-1}	K_2, M^{-1}	ΔG_2, kcal-mol^{-1}	Γ_m, mg g^{-1} (mmol g^{-1})
OAC	980	−4.08	8.4	−1.26	6.02 (0.43)
300AC	840	−3.99	11.2	−1.43	5.87(0.42)
400AC	560	−3.75	18.2	−1.72	4.63(0.33)
500AC	560	−3.75	22.4	−1.84	3.83(0.27)
Working potentials[b]	K_1, M^{-1}		K_2, M^{-1}		Γ_m, mg g^{-1} (mmol g^{-1})
−0.01 V	280	−3.34	33.6	−2.08	0.71 (0.05)
−0.1 V	294	−3.37	29.4	−2.00	1.00(0.07)
−0.5 V	840	−3.99	21.0	−1.80	1.43(0.10)
−1.0 V	980	−4.08	8.4	−1.26	6.1(0.44)
−1.5 V	1260	−4.32	9.8	−1.35	5.5(0.39)

[a] Electrosorption performed at −0.1 V (vs. Hg/HgO).
[b] Charging test using OAC/Ni electrode.

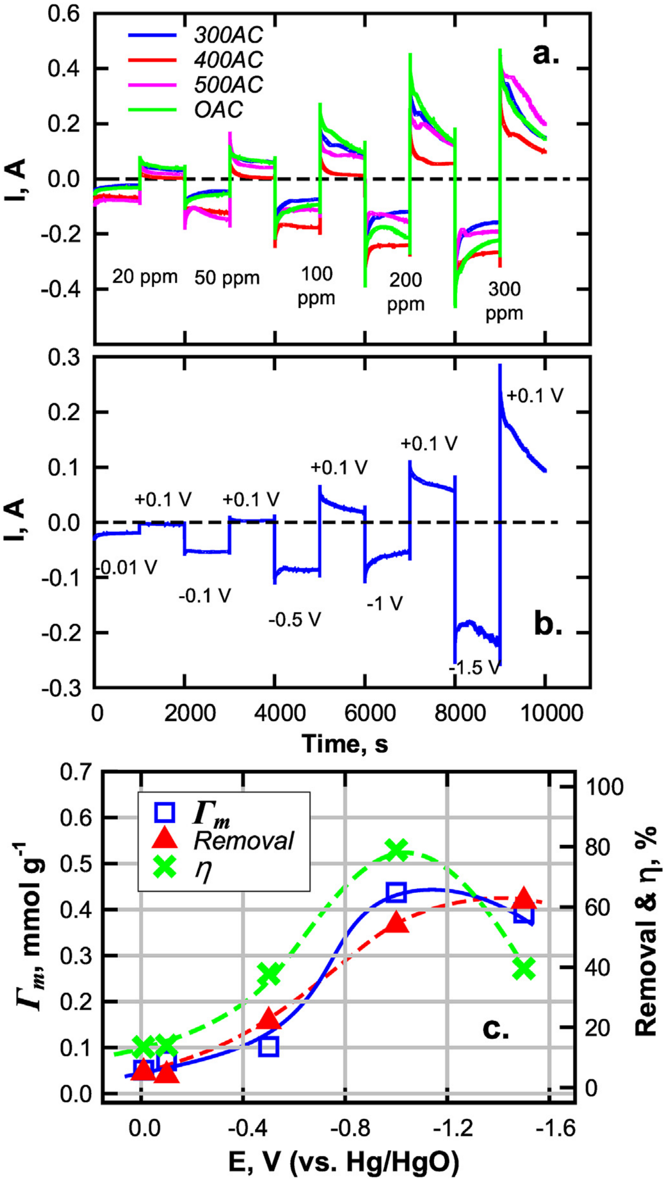

Fig. 4. Current profiles of ACs/Ni in electrolytes containing (a) ammonium ions of various initial concentrations under a constant potential −1.0 V, and (b) 50 mg-N L^{-1} by different working potentials (vs. Hg/HgO). (c) Effect of working potential on the maximum capacity, removal of NH_4^+ and current efficiency using OAC/Ni electrode.

evolution ($4H_2O + 2e^- = H_2 + 2OH^-$) must occur at higher overpotential than that of simple ions storage in the double-layer structure (Zhang et al., 2018). Nevertheless, the metallic Ni foam, selected as the base for immobilizing AC, was characterized to be active in electrochemical H_2 production. As shown in Fig. S5, there was a faradaic current steeply rose at an onset potential of around −0.8 V, which was ascribed to H_2O reduction. The charge efficiency therefore decreased to 40% at −1.5 V although the removal of NH_4^+ was enhanced to 60% still. On the other hand, since the potential applied to the working Ni/AC electrode was based on Hg/HgO reference, the exact potential on the counter (Ti/IrO_2) was unpredictable. Ideally, Ti/IrO_2 may account for the removal of sulfate ions during NH_4^+ adsorption on the Ni/AC. However, according to the desorption data, the majority of NH_4^+ was desorbed into the solution when the working potential was reversed to +0.1 V (Fig. S3 & S4). Besides, since the capacitive charging current of Ti/IrO_2 was much smaller than that of the AC/Ni electrode under some electrolyte conditions (Fig. S6), NH_4^+ adsorption on DSA during CDI process should be negligible.

Table 3 shows the ammonium adsorption capacity of different materials, including biochars, activated carbons, minerals, and electrosorption on carbon-based materials. A total of three types of adsorbents, including (1) biochar (Wang et al., 2015; Li et al., 2017; Vu et al., 2017), (2) carbon based material (Vassileva et al., 2009; Moradi, 2016), and (3) mineral (mainly silicates) (Buragohain et al., 2013; Wang et al., 2018) were compared. Biochar and carbon have shown remarkable performance in adsorbing NH_4^+ due mostly to high specific surface area (around 200 m^2-g^{-1} and 1000 m^2-g^{-1} for biochar and activated carbon, respectively) and the endowed surface functional groups (by acid or H_2O_2). Mineral-type adsorbent had relatively low surface area and porosity, while the capacity of electrostatic adsorption was dependent on the cation exchange capacity (CEC). Simple conventional adsorption process required long retention time therefore large space to accommodate the treatment facility, i.e., columns/reactors, as well as strong acid or base for regeneration of spent adsorbent. Carbon-based electrodes such as graphene, active carbon, and carbon aerogel, are electrically conductive and can be readily applied in capacitive deionization (CDI) (Wimalasiri et al., 2015). As a whole, the ammonium adsorption capacity does not differ much among typical adsorbents reported in the literature. Nevertheless, CDI system, endowed with several advantages, such as low gas evolution overpotential, low cost, free from using chemicals for desorption/regeneration, high adsorption capacity, and short retention time, e.g., 5-7 mg-N g^{-1} and 20 min, respectively, in the present work, will be a promising

Table 3
Comparison adsorption and electro-sorption of ammonium ions.

	Properties	Adsorption Capacity	Ref.
Biochar			
Maple wood	Oxidized with H_2O_2, 250 m^2 g^{-1}	1–5 mg g^{-1}, desorption with 2 M KCl	Wang et al. (2015)
Corncob	Modified with HNO_3, <1 m^2 g^{-1}	20 mg g^{-1}	Vu et al. (2017)
Sugarcane	MgO impregnated, 40–200 m^2 g^{-1}	22 mg g^{-1}	Li et al. (2017)
Carbons			
AC (one-step steam)	Oxidized with H_2O_2 & HNO_3, 200–1000 m^2 g^{-1}	10–30 mg g^{-1}	Vassileva et al. (2009)
MWCN	5–30 nm length, 1–2 nm diameter, 400 m^2 g^{-1}	9.3 mg g^{-1}	Moradi (2016)
Mineral (silicate)			
Zeolite	Halloysite-made NaA, 79.6 m^2 g^{-1}	44.3 mg g^{-1}	Wang et al. (2018)
Bentonite/Kaoline	10–20 m^2 g^{-1}; CEC = 4–80 meq 100 g^{-1}	2–20 mg g^{-1}	Buragohain et al. (2013)
Electro-sorption (electrodes)			
Graphene laminates	417 m^2 g^{-1}, 1.2 nm thickness, 5.2 nm pore size, 0.54 m^3 g^{-1} pore volume	15.3 mg g^{-1}	Wimalasiri et al. (2015)
Ni foam-supported activated carbon	AC made from vegetable sponge, 1000–1500 m^2 g^{-1}, 0.5 −1 m^3 g^{-1}	5–7 mg g^{-1} (1.0 V vs. Hg/HgO), current efficiency = 80%	Present work

alternative to conventional NH_4^+ adsorption processes.

4. Conclusion

The electrosorption of NH_4^+ on activated carbon supported on Ni foam (AC/Ni) electrodes was studied. Pre-pyrolysis temperature significantly modified the intrinsic properties of AC in crystallinity, mesoporosity, and charging current, which tended to influence the adsorption capacity of NH_4^+. Results indicated that AC prepared without carbonization but activation with $ZnCl_2$ at 800 °C (i.e., OAC) had more disordered structure, higher BET surface area (>1500 $m^2 g^{-1}$), and specific capacitance (~150 $F g^{-1}$ in 0.1 M Na_2SO_4) than that of all AC samples prepared with pyrolytic carbonation. Results of batch adsorption experiments demonstrated that electrosorption of NH_4^+ onto AC/Ni electrodes reached equilibrium in 40 min at an applied potential of −1.0 V (vs. Hg/HgO), and desorption was relatively fast at an applied potential of +0.1 V(vs. Hg/HgO). A multilayer adsorption model was used to describe the electrosorption of NH_4^+. The maximum NH_4^+ adsorption capacity and the charge efficiency was >6 mg-N g^{-1} and 80%, respectively, over the OAC/Ni electrode. AC electrodes made of loofah sponge, having low ash content and high mesoporosity, were competitive in the electrosorption of aqueous NH_4^+ over conventional adsorption processes.

Acknowledgements

This work was supported by The Ministry of Science and Technology (MOST) – Taiwan, under Contract No. 107-2221-E-110 -001 -MY3. The authors also wish to thank National Sun Yat-sen University and National Kaohsiung University of Science and Technology, Taiwan, for financial support of this research under contract number NKUSTNSYSU 107-P07. Addition support was provided by US NSF IOA (1632899) to CPH.

Appendix A. Supplementary data

Supplementary data to this article can be found online at https://doi.org/10.1016/j.chemosphere.2019.125259.

References

Afif, A., Radenahmad, N., Cheok, Q., Shams, S., Kim, J.H., Azad, A.K., 2016. Ammonia-fed fuel cells: a comprehensive review. Renew. Sustain. Energy Rev. 60, 822–835.

Allwar, A., Noor, B.M., Nawi, M.A.B.M., 2008. Textural characteristics of activated carbons prepared from oil palm shells activated with $ZnCl_2$ and pyrolysis under nitrogen and carbon dioxide. J. Phys. Sci. 19, 93–104.

Alothman, Z.A., 2012. A review: fundamental aspects of silicate mesoporous materials. Materials 5, 2874–2902.

Arenas, L.F., de León, C.P., Walsh, F.C., 2019. Three-dimensional porous metal electrodes: fabrication, characterisation and use. Curr. Opin. Electrochem. 16, 1–9.

Ariharan, A., Viswanathan, B., Nandhakumar, V., 2016. Hydrogen storage on boron substituted carbon materials. Int. J. Hydrogen Energy 41, 3527–3536.

Avraham, E., Noked, M., Bouhadana, Y., Soffer, A., Aurbach, D., 2010. Limitations of charge efficiency in capacitive deionization processes III: the behavior of surface oxidized activated carbon electrodes. Electrochim. Acta 56, 441–447.

Boo, C., Lee, J., Elimelech, M., 2016. Omniphobic polyvinylidene fluoride (PVDF) membrane for desalination of shale gas produced water by membrane distillation. Environ. Sci. Technol. 50, 12275–12282.

Brown, M.A., Goel, A., Abbas, Z., 2016. Effect of electrolyte concentration on the stern layer thickness at a charged interface. Angew. Chem. Int. Ed. 55, 3790–3794.

Buragohain, P., Sredeep, S., Saiyouri, N., 2013. A study on the adsorption of ammonium in bentonite and kaolinite. Int. J. Chem. Environ. Biolog. Sci. 1 (1), 157–160.

Chang, C.C., Kazoe, Y., Morikawa, K., Mawatari, K., Yang, R.J., Kitamori, T., 2013. Numerical simulation of proton distribution with electric double layer in extended nanospaces. Anal. Chem. 85, 4468–4474.

Cheng, T.H., Huang, C.P., Huang, Y.H., Shih, Y.J., 2017. Kinetic study and optimization of electro-Fenton process for dissolution and mineralization of ion exchange resins. Chem. Eng. J. 308, 954–962.

Dai, M., Xia, L., Song, S., Peng, C., Rangel-Mendeze, J.R., Cruz-Gaona, R., 2018. Electrosorption of As(III) in aqueous solutions with activated carbon as the electrode. Appl. Surf. Sci. 434, 816–821.

Danish, M., Ahmad, T., 2018. A review on utilization of wood biomass as a sustainable precursor for activated carbon production and application. Renew. Sustain. Energy Rev. 87, 1–21.

Diehl, B.G., Brown, N.R., Frantz, C.W., Lumadue, M.R., Cannon, F., 2013. Effects of pyrolysis temperature on the chemical composition of refined softwood and hardwood lignins. Carbon 60, 531–537.

Garcia-Segura, S., Lanzarini-Lopes, M., Hristovski, K., Westerhoff, P., 2018. Electrocatalytic reduction of nitrate: fundamentals to full-scale watertreatment applications. Appl. Catal. B Environ. 236, 546–568.

Golub, D., Oren, Y., Soffer, A., 1987. The electrical double layer of carbon and graphite electrodes, Part IV. Dependence of carbon electrode dimensions and electrical capacity on pH. J. Electroanal. Chem. 221, 41–53.

Hameed, B.H., Din, A.T.M., Ahmad, A.L., 2007. Adsorption of methylene blue onto bamboo-based activated carbon: kinetics and equilibrium studies. J. Hazard Mater. 141, 819–825.

Harned, H.S., Owen, B.B., 1959. The Physical Chemistry of Electrolytic Solutions, third ed. Reinhold Pub. Corp., New York, NY. p. 600.

Hauck, M., Maalcke-Luesken, F.A., Jetten, M.S.M., Huijbregts, M.A.J., 2016. Removing nitrogen from wastewater with side stream anammox: what are the trade-offs between environmental impacts? Resour. Conserv. Recycl. 107, 212–219.

Helfferich, F., 1962. Ion Exchange. McGraw-Hill Book Company, Inc., New York, NY, p. 198.

Hu, Z., Srinivasan, M.P., Ni, Y., 2001. Novel activation process for preparing highly microporous and mesoporous activated carbons. Carbon 39, 877–886.

Huang, Z., Lu, L., Cai, Z., Ren, Z.J., 2016. Individual and competitive removal of heavy metals using capacitive deionization. J. Hazard Mater. 302, 323–331.

Kim, T., Dykstra, J.E., Porada, S., van der Wal, A., Yoon, J., Biesheuvel, P.M., 2015. Enhanced charge efficiency and reduced energy use in capacitive deionization by increasing the discharge voltage. J. Colloid Interface Sci. 446, 317–326.

Kressman, T.R.E., Kitchner, J.A.J., 1949. Cation exchange with a synthetic phenosulphoate resin. 1. Equilibrium with univalent cations. J. Chem. Soc. 1190, 1201.

Kumar, R., Gupta, S.S., Katiyar, S., Raman, V.K., Varigala, S.K., Pradeep, T., Sharma, A., 2016. Carbon aerogels through organo-inorganic co-assembly and their application in water desalination by capacitive deionization. Carbon 99, 375–383.

Lacey, M.J., Jeschull, F., Edström, K., Brandell, D., 2014. Porosity blocking in highly porous carbon black by PVdF binder and its implications for the Li–S system. J. Phys. Chem. C 118, 25890–25898.

Laxman, K., Myint, M.T.Z., Bourdoucen, H., Dutta, J., 2014. Enhancement in ion adsorption rate and desalination efficiency in a capacitive deionization cell through improved electric field distribution using electrodes composed of activated carbon cloth coated with zinc oxide nanorods. ACS Appl. Mater. Interfaces 6, 10113–10120.

Lee, B., Park, N., Kang, K.S., Ryu, H.J., Hong, S.H., 2018. Enhanced capacitive deionization by dispersion of CNTs in activated carbon electrode. ACS Sustain. Chem. Eng. 6 (2), 1572–1579.

Li, R., Wang, J.J., Zhou, B., Zhang, Z., Liu, S., Lei, S., Xiao, R., 2017. Simultaneous capture removal of phosphate, ammonium and organic substances by MgO impregnated biochar and its potential use in swine wastewater treatment. J. Clean. Prod. 147, 96–107.

Li, J., Ji, B., Jiang, R., Zhang, P., Chen, N., Zhang, G., Qu, L., 2018. Hierarchical hole-enhanced 3D graphene assembly for highly efficient capacitive deionization. Carbon 129, 95–103.

Lozano-Castello, D., Lillo-Rodenas, M.A., Cazorla-Amoros, D., Linares-Solano, A., 2001. Preparation of activated carbons from Spanish anthracite I. Activation by KOH. Carbon 39, 741–749.

Ma, D., Wang, Y., Han, X., Xu, S., Wang, J., 2017. Electrode configuration optimization of capacitive deionization cells based on zero charge potential of the electrodes. Separ. Purif. Technol. 189, 467–474.

Moradi, O., 2016. Applicability comparison of different models for ammonium ion adsorption by multi-walled carbon nanotube. Arabian J. Chem. 9, S1170–S1176.

Omosebi, A., Gao, X., Landon, J., Liu, K., 2014. Asymmetric electrode configuration for enhanced membrane capacitive deionization. ACS Appl. Mater. Interfaces 6, 12640–12649.

Oren, Y., Tobias, H., Soffer, A., 1984. The electrical double-layer of carbon and graphite, Part I. Dependence of electrolyte type and concentration. J. Electroanal. Chem. 162, 87–99.

Park, L.K., Satinover, S.J., Yiacoumi, S., Mayes, R.T., Borole, A.P., Tsouris, C., 2018. Electrosorption of organic acids from aqueous bio-oil and conversion into hydrogen via microbial electrolysis cells. Renew. Energy 125, 21–31.

Porada, S., Zhao, R., van der Wal, A., Presser, V., Biesheuvel, P.M., 2013. Review on the science and technology of water desalination by capacitive deionization. Prog. Mater. Sci. 58, 1388–1442.

Sarvajith, M., Reddy, G.K.K., Nancharaiah, Y.V., 2018. Textile dye biodecolourization and ammonium removal over nitrite in aerobic granular sludge sequencing batch reactors. J. Hazard Mater. 342, 536–543.

Shih, Y.J., Chen, K.H., Huang, Y.H., 2014. Mineralization of organic acids by the photo-electrochemical process in the presence of chloride ions. J. Taiwan Inst. Chem. Eng. 45, 962–966.

Shih, Y.J., Huang, Y.H., Huang, C.P., 2018b. In-situ electrochemical formation of nickel oxyhydroxide (NiOOH) on metallic nickel foam electrode for the direct oxidation of ammonia in aqueous solution. Electrochim. Acta 281, 410–419.

Shih, Y.J., Su, C.C., Huang, C.P., 2015. The synthesis, characterization, and application of a platinum modified graphite electrode (Pt/G) exemplified by chloride oxidation. Separ. Purif. Technol. 156, 961–971.

Shih, Y.J., Huang, Y.H., Huang, C.P., 2017. Oxidation of ammonia in dilute aqueous solutions over graphite-supported a- and b-lead dioxide electrodes (PbO_2@G). Electrochim. Acta 257, 444–454.

Shih, Y.J., Huang, Y.H., Huang, C.P., 2018a. Electrocatalytic ammonia oxidation over a nickel foam electrode: role of $Ni(OH)_{2(s)}$-$NiOOH_{(s)}$ nanocatalysts. Electrochim. Acta 263, 261–271.

Shih, Y.J., Dong, C.D., Huang, Y.H., Huang, C.P., 2019. Electro-sorption of ammonium ion onto nickel foam supported highly microporous activated carbon prepared from agricultural residues (dried Luffa cylindrica). Sci. Total Environ. 673, 296–305.

Simaioforidou, A., Papastergiou, M., Margellou, A., Petrakis, D., Louloudi, M., 2017. Activated vs. pyrolytic carbon as support matrix for chemical functionalization: efficient heterogeneous non-heme Mn(II) catalystsfor alkene oxidation with H_2O_2. J. Mol. Catal. 426, 516–525.

Song, Q., Li, M., Wang, L., Ma, X., Liu, F., Liu, X., 2019. Mechanism and optimization of electrochemical system for simultaneous removal of nitrate and ammonia. J. Hazard Mater. 363, 119–126.

Stewart, B.M., 1985. Effect of temperature on the formation of indophenol blue in a spectrophotometric method for the determination of ammonia. Water Res. 19, 1443–1445.

Suhas, Gupta, V.K., Carrott, P.J.M., Singh, R., Chaudhary, M., Kushwaha, S., 2016. Cellulose: a review as natural, modified and activated carbon adsorbent. Bioresour. Technol. 216, 1066–1076.

Tan, W.C., Saw, L.H., Thiam, H.S., Xuan, J., Cai, Z., Yew, M.C., 2018. Overview of porous media/metal foam application in fuel cells and solarpower systems. Renew. Sustain. Energy Rev. 96, 181–197.

Tang, W., Kovalsky, P., He, D., Waite, T.D., 2015. Fluoride and nitrate removal from brackish groundwaters by batch-mode capacitive deionization. Water Res. 84, 342–349.

Teng, H., Yeh, T.S., 1998. Preparation of activated carbons from bituminous coals with zinc chloride activation. Ind. Eng. Chem. Res. 37, 58–65.

Thakur, A.K., Choudhary, R.B., Majumder, M., Gupta, G., 2017. In-Situ Integration of waste coconut shell derived activated carbon/polypyrrole/rare earth metal oxide (Eu_2O_3): a novel step towards ultrahigh volumetric capacitance. Electrochim. Acta 251, 532–545.

Vassileva, P., Tzvetkova, P., Nickolov, R., 2009. Removal of ammonium ions from aqueous solutions with coal-based activated carbons modified by oxidation. Fuel 88, 387–390.

Vu, T.M., Trinh, V.T., Doan, D.P., Van, H.T., Nguyen, T.V., Vigneswaran, S., Ngo, H.H., 2017. Removing ammonium from water using modified corncob-biochar. Sci. Total Environ. 579, 612–619.

Wang, B., Lehmann, J., Hanley, K., Hestrin, R., Enders, A., 2015. Adsorption and desorption of ammonium by maple wood biochar as a function of oxidation and pH. Chemosphere 138, 120–126.

Wang, M., Xie, R., Chen, Y., Pu, X., Jiang, W., Yao, L., 2018. A novel mesoporous zeolite-activated carbon composite as an effective adsorbent for removal of ammonia-nitrogen and methylene blue from aqueous solution. Bioresour. Technol. 268, 726–732.

Wimalasiri, Y., Mossad, M., Zou, L., 2015. Thermodynamics and kinetics of adsorption of ammonium ions by graphene laminate electrodes in capacitive deionization. Desalination 357, 178–188.

Wrobel-Iwaniec, I., Diez, N., Gryglewicz, G., 2015. Chitosan-based highly activated carbons for hydrogen storage. Int. J. Hydrogen Energy 40, 5788–5796.

Yahya, M.A., Al-Qodah, Z., Ngah, C.W.Z., 2015. Agricultural bio-waste materials as potential sustainable precursors used for activated carbon production: a review. Renew. Sustain. Energy Rev. 46, 218–235.

Ye, Y., Ngo, H.H., Guo, W., Liu, Y., Chang, S.W., Nguyen, D.D., Liang, H., Wang, J., 2018. A critical review on ammonium recovery from wastewater for sustainable wastewater management. Bioresour. Technol. 268, 749–758.

Yuan, X.Z., Choi, S.W., Jang, E., Lee, K.B., 2018. Chemically activated microporous carbons derived from petroleum coke: performance evaluation for CF_4 adsorption. Chem. Eng. J. 336, 297–305.

Zhang, M., Zhang, H., Xu, D., Han, L., Niu, D., Zhang, L., Wu, W., Tian, B., 2011. Ammonium removal from aqueous solution by zeolites synthesized from low-calcium and high-calcium fly ashes. Desalination 277, 46–53.

Zhang, C., He, D., Ma, J., Tang, W., Waite, T.D., 2018. Faradaic reactions in capacitive deionization (CDI) - problems and possibilities: a review. Water Res. 128, 314–330.

Zhou, Y., Candelaria, S.L., Liu, Q., Uchaker, E., Cao, G., 2015. Porous carbon with high capacitanceand graphitization through controlled addition and removal of sulfur-containing compounds. Nano Energy 12, 567–577.

Zornitta, R.L., Ruotolo, L.A.M., 2018. Simultaneous analysis of electrosorption capacity and kinetics for CDI desalination using different electrode configurations. Chem. Eng. J. 332, 33–41.